

Reconstruction of Horizontal Plasma Motions at the Photosphere from Intensitygrams: A Comparison Between DeepVel, LCT, FLCT and CST

Benoit Tremblay¹ · Thierry Roudier² ·
Michel Rieutord² · Alain Vincent¹

© Springer ●●●

Abstract Direct measurements of plasma motions at the photosphere are limited to the line-of-sight component of the velocity. Several algorithms were consequently developed to reconstruct the transverse components from observed continuum images or magnetograms. We compare the space and time averages of horizontal velocity fields at the photosphere inferred from pairs of consecutive intensitygrams by the LCT, FLCT and CST methods and the DeepVel neural network in order to identify the method best suited for generating synthetic observations to be used for data assimilation. The Stein and Nordlund (*Astrophys. J. Lett.* **753**, L13, 2012) magneto-convection simulation is used to generate synthetic SDO/HMI intensitygrams and reference flows to train DeepVel. Inferred velocity fields show that DeepVel best performs at subgranular and granular scales and is second only to FLCT at mesogranular and supergranular scales.

Keywords: Photosphere · Velocity fields, Photosphere · Granulation

1. Introduction

Numerical simulations of solar convection are capable of evolving granulation patterns (Stein and Nordlund, 2012; Abbett and Fisher, 2012; Vögler *et al.*, 2005) and active region emergences (Jiang *et al.*, 2016; Rempel and Cheung, 2014) that are consistent with observations over short time scales within domains ranging from the upper convection zone to lower corona. Recent models even find energy variations that are consistent with the production of eruptive events (*e.g.*,

¹ Département de Physique, Université de Montréal,
C.P. 6128, Succ. A, Montréal, Québec H3C 3J7, Canada.

Email: benoit@astro.umontreal.ca

Email: vincent@astro.umontreal.ca

² IRAP, Université de Toulouse, CNRS, UPS, CNES,
Toulouse, France.

Email: thierry.roudier@irap.omp.eu

Email: michel.rieutord@irap.omp.eu

Rempel, 2017) and have realistically simulated the onset of a flare through data-driven simulations (*e.g.*, Jiang *et al.*, 2016). The next logical step for realistic simulations would be to attempt to predict the short term evolution of the Sun’s photosphere for space weather modelling through data assimilation (*e.g.*, Abbett and Fisher, 2010). Data assimilation combines observations with model predictions (the background) in order to adjust the model’s initial state and produce improved forecasts (Bouttier and Courtier, 1999). MHD model variables typically include components of the magnetic field [\mathbf{B}] and plasma motions [\mathbf{v}] (or momentum [\mathbf{p}]), and a combination of the gas density [ρ], pressure [P], temperature [T] and internal energy density [e] coupled through an equation of state (Abbett, 2007). Satellite and ground-based observations can resolve subgranular features over time scales shorter than one granule turnover time. They are however limited to the Sun’s photosphere and may not satisfy the model’s equations (Abbett and Fisher, 2010). The Doppler effect allows for the direct measurement of the line-of-sight component of plasma proper motions at the photosphere, *e.g.* Doppler velocities. For the transverse component, reconstructions are the only available source of information. Near disk center, spherical distortion is negligible and Doppler velocities measure the vertical component of plasma motions. As we move away from disk center, Doppler velocities acquire an increasingly important horizontal component. At the solar limb, measured motions are essentially horizontal. In order to use inferred velocity fields as synthetic observations for data assimilation, reconstruction algorithms must quickly and reliably compute the flow’s amplitude and direction at spatial and temporal scales that are consistent with the model or other available observations.

Local Correlation Tracking (LCT: November and Simon, 1988), Fourier-based Local Correlation Tracking (FLCT: Fisher and Welsch, 2008) and Coherent Structure Tracking (CST: Rieutord *et al.*, 2007) use consecutive intensitygrams to estimate *optical flows* at the photosphere, *i.e.* the velocity field that should be applied to an image (*e.g.* a continuum image) to connect it to its counterpart at a later time (Fisher and Welsch, 2008). CST is a granule tracking technique which produces good estimates of the flow’s amplitude when resampled to supergranular scales (Rieutord *et al.*, 2007). LCT and FLCT account for both granules and intergranules when cross-correlating continuum images and best estimate the field’s direction at mesogranular and supergranular scales (Fisher and Welsch, 2008), with LCT underestimating the amplitude (Verma, Steffen, and Denker, 2013). Alternatively, algorithms such as MEF (Longcope, 2004) and DAVE (Schuck, 2006) use consecutive Dopplergrams and magnetograms and solve the vertical component of the magnetic induction equation to infer the motions of magnetic footpoints at the photosphere. MEF-R (Tremblay and Vincent, 2015, 2016) expanded on the concept of MEF by also adjusting a local eddy magnetic diffusivity to account for subgrid physics. Although optical flows do not represent actual horizontal plasma motions, they were found to be highly correlated with plasma velocity fields at scales larger than 2.5 Mm (Rieutord *et al.*, 2001). This correlation is further improved by computing time averages of the inferred instantaneous velocities (Rieutord *et al.*, 2001).

DeepVel (Asensio Ramos, Requerey, and Vitas, 2017) is a deep fully convolutional neural network used to infer instantaneous local (pixel-to-pixel) horizontal

velocities at three optical depths from pairs of intensitygrams. It does not require space and time averaging for improved results unlike other intensity-based reconstruction algorithms. Continuum images at optical depth $[\tau = 1]$ and corresponding horizontal plasma motions at $\tau = \{1, 0.1, 0.01\}$ are extracted from an MHD model of the Sun’s photosphere and atmosphere and are used as synthetic observations to train the neural network through deep learning. Inferred velocities are thus highly dependent on the model data used for training. To generate horizontal velocities at different spatial resolutions, cadences, positions on the solar disk and/or radii, a new version of the DeepVel neural network must be trained using model data with those specific properties. In this paper, two versions of the neural network were trained.

A comparison between time and space averages of the velocity fields reconstructed from intensitygrams using LCT, FLCT, CST and DeepVel is presented. The article is organized as follows: data preprocessing and training of the DeepVel neural network are described in Section 2. Reconstructions of horizontal velocities at the photosphere from synthetic SDO/HMI observations are compared in Section 3. We conclude in Section 4.

2. Data Preprocessing and Neural Network Training

The *Helioseismic Magnetic Imager* (HMI: Schou *et al.*, 2012) onboard the *Solar Dynamics Observatory* (SDO) spacecraft produces full-disk Dopplergrams, intensitygrams and magnetograms with spatial resolution $[\Delta x \approx 0.505'' \approx 368 \text{ km}]$ per pixel every $[\Delta t = 45 \text{ s}]$ (Hoeksema *et al.*, 2014). Although the spatial resolution is insufficient to resolve subgranular features, SDO/HMI data may prove useful when attempting to predict the short term evolution of granulation and active regions and the occurrence of solar flares (Bobra *et al.*, 2014). From these observations, additional quantities can be inferred at the photosphere such as the local temperature (*e.g.*, Solanki, Walther, and Livingston (1993)) and horizontal velocities $[\mathbf{v}]$, all of which could be included as synthetic observations in data assimilation processes. For this purpose, the DeepVel neural network is trained using synthetic SDO/HMI data.

The Stein and Nordlund (2012) magneto-convection simulation produces 1008 by 1008 pix^2 maps of the continuum intensity $[I_c]$ (Figure 1(a)), vector magnetic field $[\mathbf{B}_S]$ and velocity field $[\mathbf{v}_S]$ of solar granulation at optical depths $\tau = \{1, 0.1, 0.01\}$ with spatial resolution $\Delta x = \Delta y = 96 \text{ km}$ per pixel and time step $\Delta t = 60 \text{ s}$. The simulation output over six hours was first convolved with the SDO/HMI PSF, as described in Diaz Baso and Asensio Ramos (2017), and then **rebinned using nearest-neighbor sampling** to produce synthetic observations with the same spatial resolution as SDO/HMI data ($\Delta x \approx 0.505'' \approx 368 \text{ km}$ per pixel). The resulting intensitygrams (Figure 1(b)) are then used as input to compute horizontal velocities (Section 3). Following the procedure described by Asensio Ramos, Requerey, and Vitas (2017), patches of 50 by 50 pixels² were randomly extracted at the same position from I_c ($\tau \approx 1$) and \mathbf{v}_S ($\tau \approx \{1, 0.1, 0.01\}$) at two consecutive time steps. The continuum intensity images were normalized by the sample’s median. The velocities were shifted by the minimum velocity and

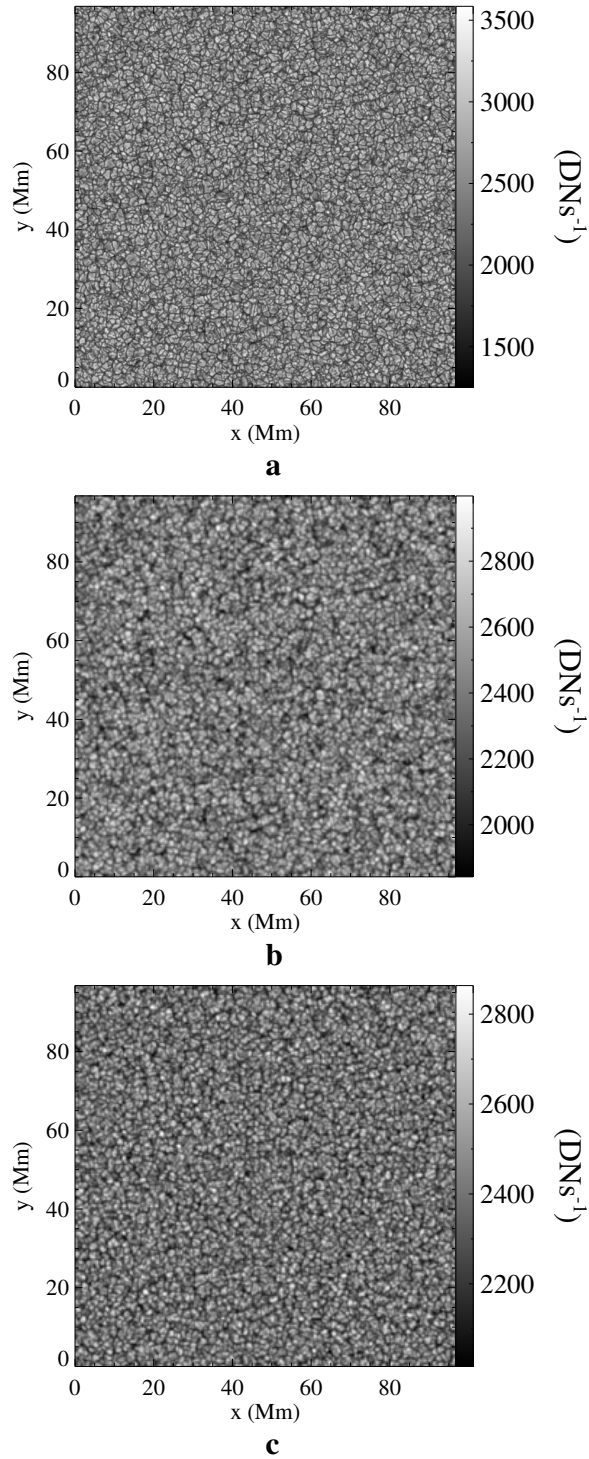


Figure 1. (a) Continuum intensity I_c ($\tau \approx 1$) as computed by the Stein and Nordlund (2012) magneto-convection simulation ($\Delta x = \Delta y = 96$ km per pixel). (b) Synthetic SDO/HMI intensitygram generated by convolving I_c ($\tau \approx 1$) by the SDO/HMI PSF and then resampling the data ($\Delta x \approx 0.505'' \approx 368$ km per pixel). (c) Synthetic SDO/HMI intensitygram following the removal of high frequencies by $k - \omega$ filtering.

Table 1. Statistics quantifying the effects of $k - \omega$ filtering on the continuum intensity I_c and horizontal velocity field \mathbf{v}_S . Fields extracted from the synthetic SDO/HMI images at a given time t are compared to their $k - \omega$ filtered counterpart. C is the Pearson correlation coefficient between the non-filtered and filtered fields, E_N is the error normalized by the norm of the mean value, E_M is the mean relative error, ϵ is the ratio of quadratic errors and C_{CS} is the Cauchy–Schwarz inequality (Schrijver *et al.*, 2006).

Fields	C	E_N	E_M	ϵ	C_{CS}
I_c ($\tau \approx 1$)	0.999	0.029	0.029	0.997	-
\mathbf{v}_S ($\tau \approx 1$)	0.859	0.510	0.610	0.628	0.810

normalized by the difference between the maximum and minimum velocities so that $v \in [0, 1]$. A total of 2000 pairs were used to train DeepVel and an extra 200 pairs were extracted for the validation process. The neural network was trained over 10 epochs using the *Tensorflow* backend and a NVIDIA 960M GPU. **Training was stopped once the network’s cost function no longer varied significantly in order to avoid overtraining.** Subsets of 20 pairs were used to estimate the gradient in the network’s minimization process.

Following the same procedure, a second version of the DeepVel neural network was trained using $k - \omega$ filtered input data. A threshold was applied to the synthetic SDO/HMI images to remove high frequencies, *i.e.* to filter out supersonic phase velocities (over 5 km s^{-1}) so that only convective motions remain (Espagnet *et al.*, 1993). This preprocessing step is carried out to evaluate whether noise filtering has any significant impact on velocity reconstructions. While the continuum images do remain highly correlated (Figures 1(b) and 1(c)), variations between filtered and non-filtered velocity fields are more significant (Table 1).

3. Results

For inferred flows to be used as synthetic observations for data assimilation, their direction and amplitude must be consistent with observations or, in this case, with a reference flow. Horizontal velocity fields computed by DeepVel [\mathbf{v}_D], LCT [\mathbf{v}_L], FLCT [\mathbf{v}_F] and CST [\mathbf{v}_C] from pairs of synthetic SDO/HMI intensitygrams are compared to the synthetic velocity field [\mathbf{v}_S] generated from the Stein and Nordlund (2012) simulation. A 7-pixel bin was used for sampling in LCT and FLCT. This value corresponds to a FWHM of approximately 2.5 Mm (the diameter of a granule) and is the smallest scale over which granule tracking methods can be used (Rieutord *et al.*, 2010). CST velocities were resampled using a 7-pixel bin. The results are averaged over 30 minutes to increase the correlation between optical flows and plasma motions and to coincide with the shortest time window over which granule tracking can be used (Rieutord *et al.*, 2008). We limit comparisons to photospheric flows ($\tau \approx 1$), *i.e.* flows at the same optical depth at which intensitygrams are produced. C is the Pearson correlation coefficient and E_M is the mean relative error. The Cauchy-Schwarz inequality [C_{CS}] is used as a metric for the global orientation between two vector fields,

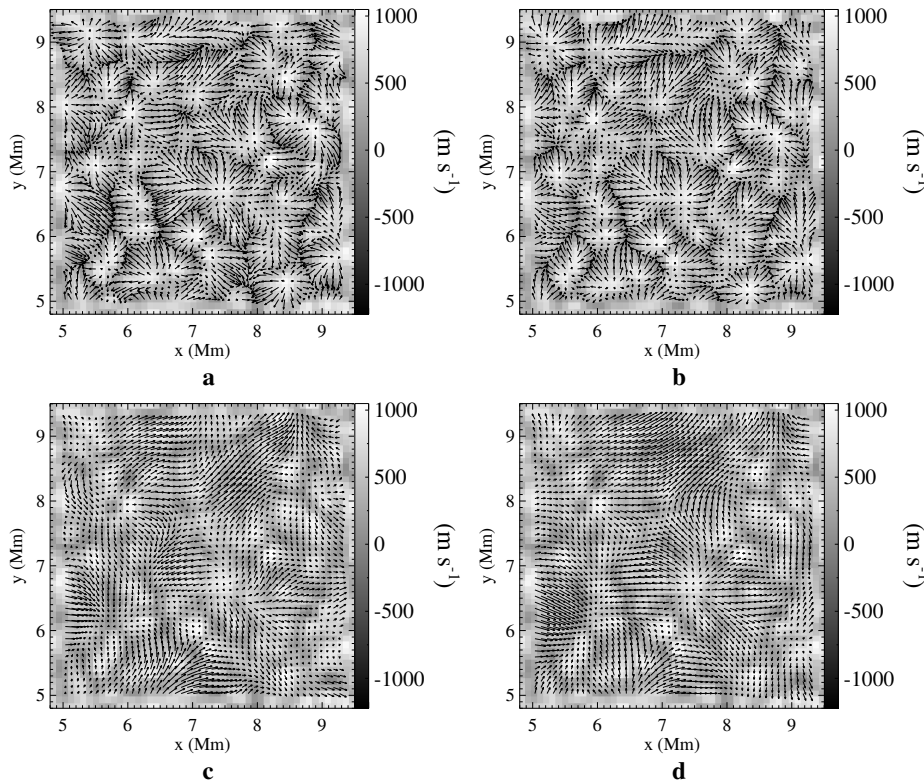


Figure 2. Patches of 50 by 50 pixels² extracted from the 30-minute averaged horizontal velocity fields (a) \mathbf{v}_S ($\tau \approx 1$), (b) \mathbf{v}_D ($\tau \approx 1$), (c) \mathbf{v}_L ($\tau \approx 1$) and (d) \mathbf{v}_F ($\tau \approx 1$) computed from pairs of consecutive synthetic intensitygrams with spatial resolution $\Delta x \approx 0.505'' \approx 368$ km per pixel. **Only the arrows of the horizontal velocity vector fields are displayed for clarity reasons.** The vertical velocity v_z ($\tau \approx 1$) computed by the Stein and Nordlund (2012) simulation is displayed as background (colorscale).

with $C_{CS} = \pm 1$ when they are parallel/anti-parallel and $C_{CS} = 0$ when they are perpendicular (Schrijver *et al.*, 2006).

3.1. Velocity Fields Inferred from Non-Filtered Synthetic Data

At granular scales, \mathbf{v}_D (Figure 2(b)) successfully reproduces the features of \mathbf{v}_S (Figure 2(a)). The flow is consistent with the overturning motion of plasma inside granules (see vertical plasma motions [v_z] displayed in the background of Figure 2). Horizontal velocity vectors diverge away from the center of granules (hot rising plasma, v_z ($\tau \approx 1$) > 0) and converge toward intergranules (cold descending plasma, v_z ($\tau \approx 1$) < 0). Table 2 also confirms that statistically, the amplitudes, orientations and horizontal divergences of \mathbf{v}_D and \mathbf{v}_S are spatially correlated. For comparisons at larger scales, a smoothing window of the same dimensions as the bin used by the LCT and FLCT methods (7 by 7 pixels²) was applied to \mathbf{v}_S and \mathbf{v}_D . The agreement between \mathbf{v}_L (Figure 2(c)), \mathbf{v}_F (Figure 2(d)), \mathbf{v}_C (not shown because of the low spatial resolution) and \mathbf{v}_S is further

Table 2. Comparison between the 30-minute averaged \mathbf{v}_S and the 30-minute averaged horizontal velocities computed by DeepVel (\mathbf{v}_D), LCT (\mathbf{v}_L), FLCT (\mathbf{v}_F) and CST (\mathbf{v}_C) at granular (G) and supergranular (SG) scales, as well as the comparison between their respective divergences ($\nabla \cdot \mathbf{v}_S$, $\nabla \cdot \mathbf{v}_D$, $\nabla \cdot \mathbf{v}_L$, $\nabla \cdot \mathbf{v}_F$ and $\nabla \cdot \mathbf{v}_C$). When comparing to \mathbf{v}_L or \mathbf{v}_F at supergranular scales, \mathbf{v}_S is smoothed using a 7 by 7 pixels² window. When comparing to \mathbf{v}_C , \mathbf{v}_S is smoothed using a 7 by 7 pixels² window and then resampled using a 7-pixel bin.

Fields	C(G)	E _M (G)	C _{CS} (G)	C(SG)	E _M (SG)	C _{CS} (SG)
$\mathbf{v}_S, \mathbf{v}_D$	0.850	0.681	0.795	0.747	1.022	0.614
$\mathbf{v}_S, \mathbf{v}_L$	0.481	0.952	0.413	0.680	0.877	0.596
$\mathbf{v}_S, \mathbf{v}_F$	0.596	0.911	0.509	0.857	0.702	0.778
$\mathbf{v}_S, \mathbf{v}_C$	0.265	1.098	0.225	0.450	1.166	0.394
$\nabla \cdot \mathbf{v}_S, \nabla \cdot \mathbf{v}_D$	0.952	1.473	-	0.964	4.805	-
$\nabla \cdot \mathbf{v}_S, \nabla \cdot \mathbf{v}_L$	0.272	1.485	-	0.554	7.588	-
$\nabla \cdot \mathbf{v}_S, \nabla \cdot \mathbf{v}_F$	0.353	1.484	-	0.751	5.883	-
$\nabla \cdot \mathbf{v}_S, \nabla \cdot \mathbf{v}_C$	0.160	2.678	-	0.270	14.20	-

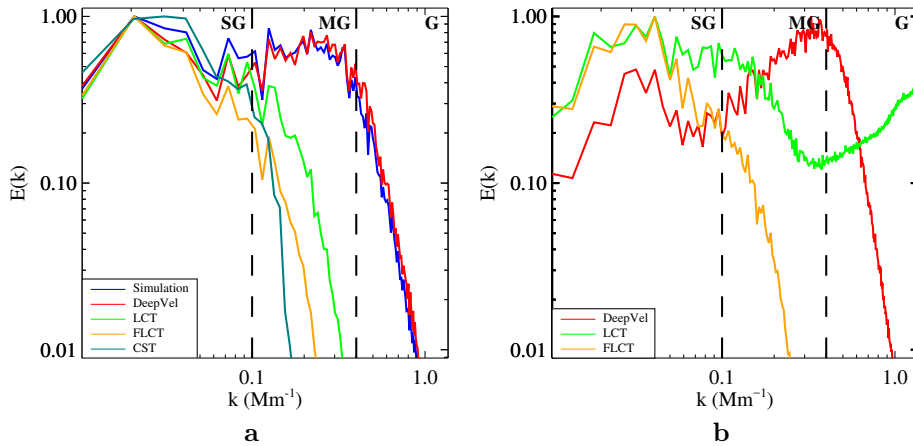


Figure 3. Kinetic energy spectra $E(k)$ of the 30-minute averaged horizontal velocities computed from (a) pairs of consecutive synthetic intensitygrams with spatial resolution $\Delta x \approx 0.505'' \approx 368$ km per pixel and (b) pairs of consecutive SDO/HMI intensitygrams. k is the wavenumber. Granular ($k \approx 1 \text{ Mm}^{-1}$), mesogranular ($k \approx 0.4 \text{ Mm}^{-1}$) and supergranular ($k \approx 0.1 \text{ Mm}^{-1}$) scales are labeled by 'G', 'MG' and 'SG' respectively.

improved when smoothed (Table 2), but granular motions are no longer resolved. FLCT performs better at large scales than LCT and CST (Table 2). The FLCT algorithm best reconstructs the large scale component of \mathbf{v}_S over 30 minutes (Table 2). The correlation is however highly dependent on the time average. For instantaneous velocities, it is DeepVel that best reconstructs flows at all scales.

3.1.1. Kinetic Energy Spectra

Signatures of the components of the plasma motions at various scales are emphasized by the kinetic energy spectra $[E(k)]$ defined as

$$\frac{1}{2} \langle \bar{v}_h^2 \rangle = \int_0^\infty E(k) dk, \quad (1)$$

where $[k]$ is the wavenumber, everywhere divided by 2π so as to easily give the associated wavelength, $[\bar{v}_h]$ is the horizontal velocity modulus averaged over thirty minutes and $\langle \cdot \rangle$ is a spatial average operator. More specifically, the kinetic energy densities $E(k)$ are obtained following

$$E(k) = \frac{N^3 p}{4\pi N_x N_y} \sum_{\forall k' \in [k, k+dk]/2\pi} |\bar{v}_h(k')|^2, \quad (2)$$

where N_x and N_y are the dimensions of the data array, N are the dimensions of the square over which Fourier transforms are performed, and p is the linear size of a pixel. We refer to Rieutord *et al.* (2010) for the detailed computation of $E(k)$. At supergranular scales ($k \leq 0.1 \text{ Mm}^{-1}$), there is a good agreement between \mathbf{v}_S and all inferred flows (Figure 3). \mathbf{v}_D (red curve) is the only velocity field which accurately reproduces the energy spectra of \mathbf{v}_S (blue curve) at mesogranular ($0.1 < k \leq 0.4 \text{ Mm}^{-1}$), granular ($0.4 < k \leq 1 \text{ Mm}^{-1}$) and subgranular scales ($k > 1 \text{ Mm}^{-1}$). The other reconstruction algorithms peak at supergranular scales and do not contribute to spectral features below mesogranular scales. This is expected since granule tracking is unable to track flows below $k \approx 0.4 \text{ Mm}^{-1}$ ($\lambda \approx 2.5 \text{ Mm}$; Rieutord *et al.*, 2010) and the bin size used by both LCT and FLCT being 7 pixels ($\approx 2.5 \text{ Mm}$) and even larger for CST.

3.1.2. Propagation of Passive Scalars

Supergranular motions were further examined through the propagation of corks by flows \mathbf{v}_S , \mathbf{v}_D and \mathbf{v}_L averaged over six hours (Figure 4). A smoothing window of the same dimensions as the bin used by the LCT method (7 by 7 pixels²) was applied to \mathbf{v}_S and \mathbf{v}_D . Positive horizontal divergences of \mathbf{v}_D and \mathbf{v}_L are spatially correlated with the reference flow \mathbf{v}_S (Pearson linear correlation coefficients of 0.922 and 0.783 respectively). Starting from randomized positions, a great majority of corks gather on the network formed by the line-of-sight photospheric magnetic field at supergranular scales (Figure 4), confirming the presence of a similar supergranular component in all three flows.

3.2. Velocity Fields Inferred from $k - \omega$ Filtered Synthetic Data

A second version of the neural network was trained using $k - \omega$ filtered synthetic SDO/HMI data. Inferred velocity fields are displayed in Figure 5. Spatial correlations, mean relative errors and orientations between all flow reconstructions and $k - \omega$ filtered \mathbf{v}_S (Table 3) remain approximately the same as between

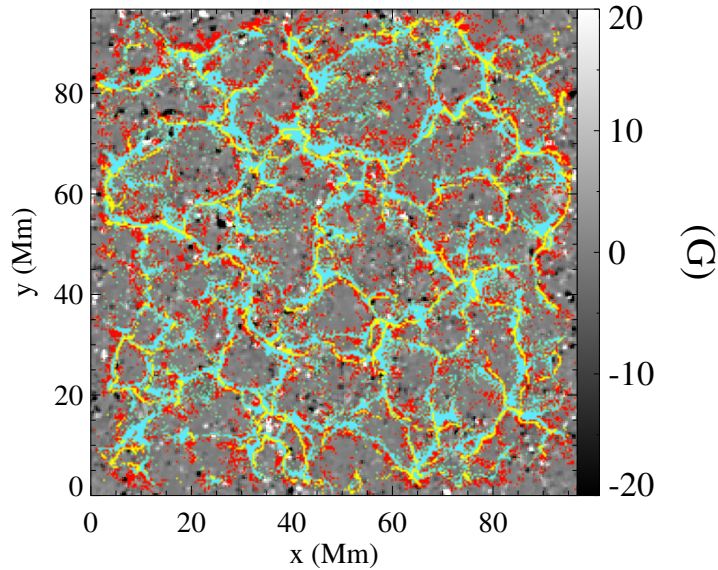


Figure 4. Location of corks over a period of six hours by \mathbf{v}_S (red), \mathbf{v}_L (blue) and \mathbf{v}_D (yellow) averaged over six hours. Velocity fields \mathbf{v}_S and \mathbf{v}_D were smoothed using a 7 by 7 pixels² window. The vertical magnetic field $B_z(\tau \approx 1)$ computed by the Stein and Nordlund (2012) simulation and resampled to $\Delta x \approx 0.505'' \approx 368$ km per pixel is displayed as background with a threshold of ± 20 G (colorscale). A majority of corks gather on the supergranular network formed by $B_z(\tau \approx 1)$.

Table 3. Comparison between the 30-minute averaged \mathbf{v}_S and the 30-minute averaged horizontal velocities computed by DeepVel (\mathbf{v}_D), LCT (\mathbf{v}_L), FLCT (\mathbf{v}_F) and CST (\mathbf{v}_C) at granular (G) and supergranular (SG) scales, as well as the comparison between their respective divergences ($\nabla \cdot \mathbf{v}_S$, $\nabla \cdot \mathbf{v}_D$, $\nabla \cdot \mathbf{v}_L$, $\nabla \cdot \mathbf{v}_F$ and $\nabla \cdot \mathbf{v}_C$). Input synthetic intensitygrams and \mathbf{v}_S were $k - \omega$ filtered to remove high frequencies. When comparing to \mathbf{v}_L or \mathbf{v}_F at supergranular scales, \mathbf{v}_S is smoothed using a 7 by 7 pixels² window. When comparing to \mathbf{v}_C , \mathbf{v}_S is smoothed using a 7 by 7 pixels² window and then resampled using a 7-pixel bin.

Fields	C(G)	E_M (G)	C_{CS} (G)	C(SG)	E_M (SG)	C_{CS} (SG)
$\mathbf{v}_S, \mathbf{v}_D$	0.890	0.627	0.841	0.726	1.732	0.638
$\mathbf{v}_S, \mathbf{v}_L$	0.436	0.961	0.370	0.642	0.889	0.567
$\mathbf{v}_S, \mathbf{v}_F$	0.572	0.859	0.489	0.838	0.730	0.761
$\nabla \cdot \mathbf{v}_S, \nabla \cdot \mathbf{v}_D$	0.956	1.414	-	0.961	1.904	-
$\nabla \cdot \mathbf{v}_S, \nabla \cdot \mathbf{v}_L$	0.253	1.258	-	0.533	2.158	-
$\nabla \cdot \mathbf{v}_S, \nabla \cdot \mathbf{v}_F$	0.349	1.378	-	0.746	1.869	-

their non-filtered counterparts (Table 2). Thus, the preprocessing step of $k - \omega$ filtering does not improve horizontal velocity field reconstructions. Non-filtered and filtered flows are, however, distinct (Table 4, Figures 2 and 5) because their input data is different (Table 1).

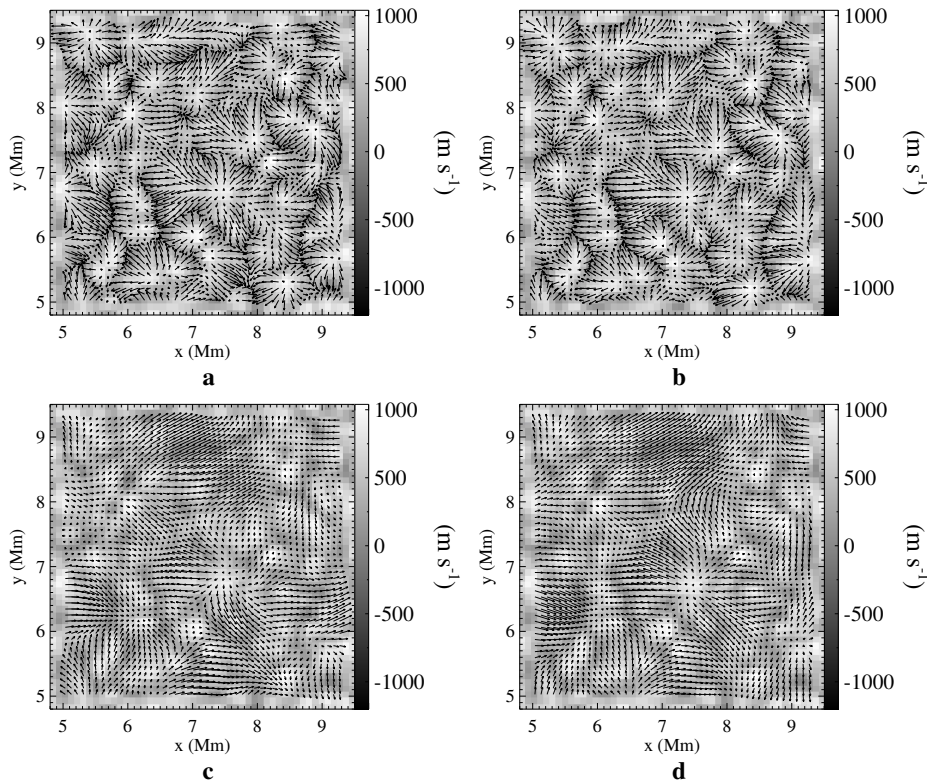


Figure 5. Patches of 50 by 50 pixels² extracted from the 30-minute averaged horizontal velocity fields (a) \mathbf{v}_S ($\tau \approx 1$), (b) \mathbf{v}_D ($\tau \approx 1$), (c) \mathbf{v}_L ($\tau \approx 1$) and (d) \mathbf{v}_F ($\tau \approx 1$) computed from pairs of consecutive synthetic intensitygrams with spatial resolution $\Delta x \approx 0.505'' \approx 368$ km per pixel and high frequencies removed by $k-\omega$ filtering. **Only the arrows of the horizontal velocity vector fields are displayed for clarity reasons.** The vertical velocity v_z ($\tau \approx 1$) computed by the Stein and Nordlund (2012) simulation and filtered for high frequencies is displayed in the background (colorscale).

Table 4. Comparison between the 30-minute averaged horizontal velocities computed from filtered and non-filtered consecutive synthetic intensitygrams with spatial resolution $\Delta x \approx 0.505'' \approx 368$ km per pixel. C is the Pearson correlation coefficient, E_N is the error normalized by the norm of the mean value, E_M is the mean relative error, ϵ is the ratio of quadratic errors and C_{CS} is the Cauchy–Schwarz inequality (Schrijver *et al.*, 2006).

Fields	C	E_N	E_M	ϵ	C_{CS}
\mathbf{v}_D	0.855	0.593	0.879	1.319	0.808
\mathbf{v}_L	0.789	0.612	0.767	0.433	0.715
\mathbf{v}_F	0.982	0.248	0.307	0.659	0.962

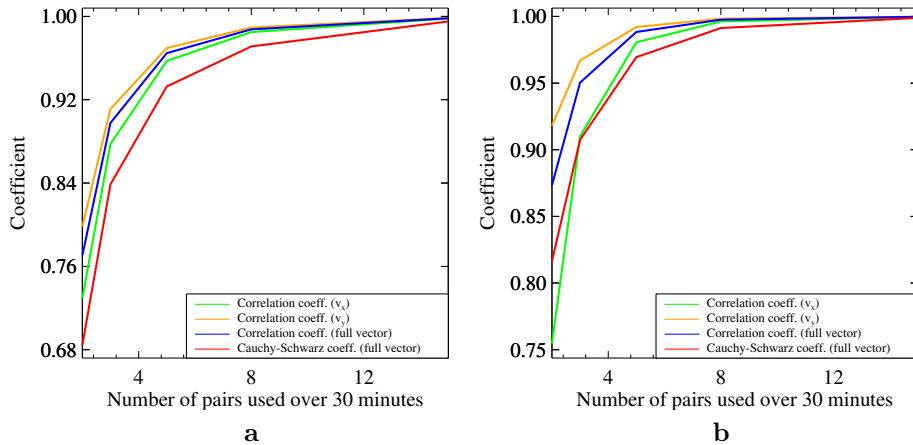


Figure 6. Evolution of the Pearson correlation coefficient and Cauchy-Schwarz inequality as a function of the number of pairs of consecutive synthetic intensitygrams used to compute the 30-minute time average of the (a) non-filtered and (b) filtered \mathbf{v}_D ($\tau \approx 1$). The reference flow used for this comparison is the 30-minute time average of \mathbf{v}_D ($\tau \approx 1$) obtained when using all available pairs.

3.3. Computation of Time Averages

To reduce the number of DeepVel computations performed in a reduction pipeline, we computed the number of evenly distributed pairs of consecutive synthetic intensitygrams that are needed to accurately estimate the 30-minute average of \mathbf{v}_D . Figure 6 displays the Pearson correlation coefficient and Cauchy-Schwarz inequality between estimates as a function of the number of pairs used out of the thirty that are available. The reference flow \mathbf{v}_D used for this comparison was computed using all available pairs. Using eight or fifteen pairs, the flow amplitudes and orientations remain accurate estimations (Figure 6(a)). This allows for faster computations of synthetic velocity fields over 30-minute intervals. The same experiment was performed using $k - \omega$ filtered synthetic intensitygrams, with no significant differences (Figure 6(b)).

3.4. Using Results from a Different Numerical Simulation as Input

To study the influence of the training set on the DeepVel-inferred velocity fields, we used as input synthetic SDO/HMI data generated from a different numerical simulation than the one used to train the neural network. More specifically, we used results of the compressible hydrodynamic convection simulation with radiative transfer used in Rieutord *et al.* (2001) and originally developed by Stein and Nordlund (1998), with spatial resolution $\Delta x = \Delta y = 95.24$ km per pixel and time step $\Delta t = 60$ s. This run differs from the Stein and Nordlund (2012) simulation by the absence of magnetic fields, the depth of the convection zone included inside the computational domain and the use of the grey approximation when treating for radiative transfer. The continuum intensities and velocity fields (Figure 7(a)) were resampled to SDO/HMI spatial resolution following

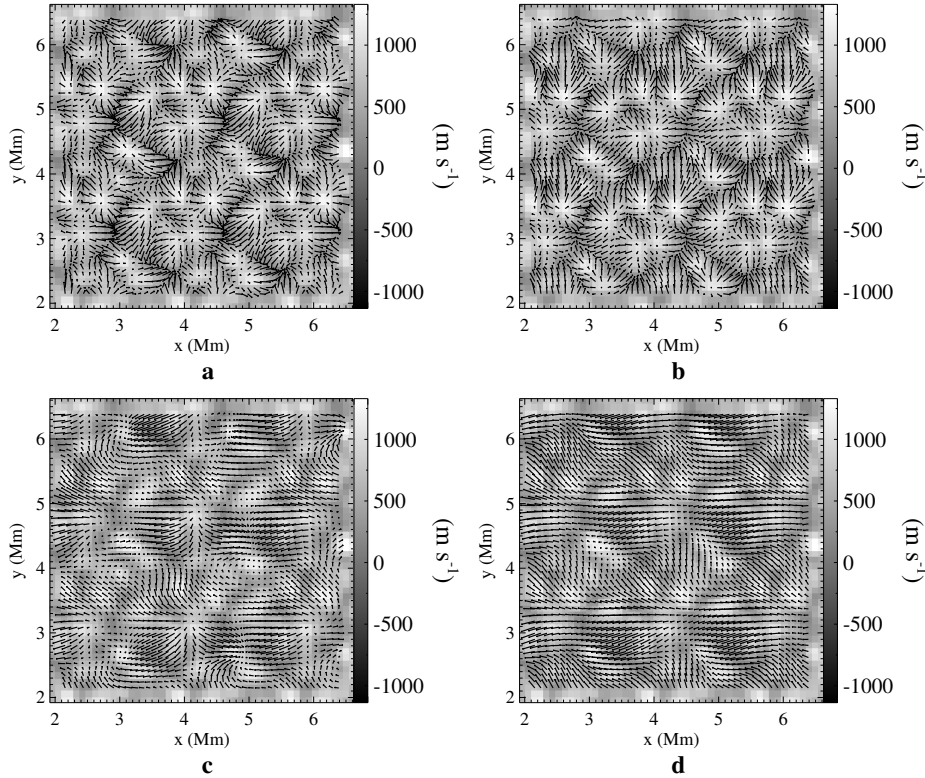


Figure 7. Patches of 50 by 50 pixels² extracted from the 30-minute averaged horizontal velocity fields (a) \mathbf{v}_S ($\tau \approx 1$), (b) \mathbf{v}_D ($\tau \approx 1$), (c) \mathbf{v}_L ($\tau \approx 1$) and (d) \mathbf{v}_F ($\tau \approx 1$) computed from pairs of consecutive synthetic intensitygrams with spatial resolution $\Delta x \approx 0.505'' \approx 368$ km per pixel. **Only the arrows of the horizontal velocity vector fields are displayed for clarity reasons.** The vertical velocity v_z ($\tau \approx 1$) generated by the Rieutord *et al.* (2001) numerical simulation is displayed as background (colorscale).

Table 5. Comparison between the 30-minute averaged \mathbf{v}_S and the 30-minute averaged horizontal velocities computed by DeepVel (\mathbf{v}_D), LCT (\mathbf{v}_L), FLCT (\mathbf{v}_F) and CST (\mathbf{v}_C) at granular (G) and supergranular (SG) scales using synthetic SDO/HMI generated from the Rieutord *et al.* (2001) numerical simulation. When comparing to \mathbf{v}_L or \mathbf{v}_F at supergranular scales, \mathbf{v}_S is smoothed using a 7 by 7 pixels² window.

Fields	C(G)	E _M (G)	C _{CS} (G)	C(SG)	E _M (SG)	C _{CS} (SG)
$\mathbf{v}_S, \mathbf{v}_D$	0.767	0.651	0.711	0.589	0.969	0.444
$\mathbf{v}_S, \mathbf{v}_L$	0.219	0.959	0.225	0.338	0.954	0.247
$\mathbf{v}_S, \mathbf{v}_F$	0.358	0.917	0.299	0.549	0.826	0.389

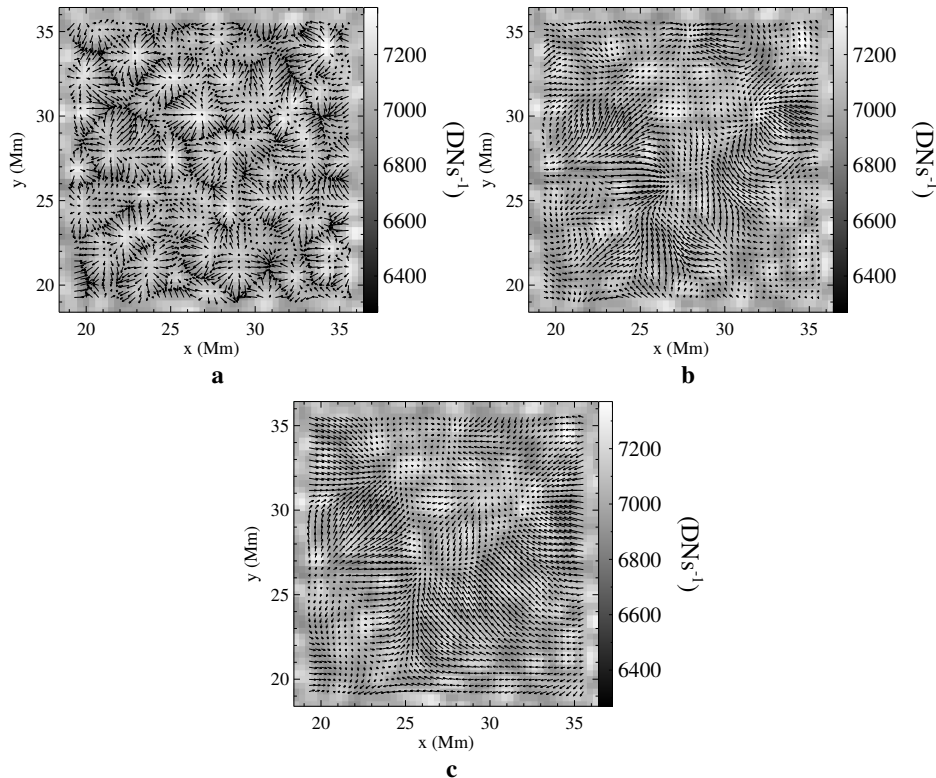


Figure 8. Patches of 50 by 50 pixels² extracted from the 30-minute averaged horizontal velocity fields (a) \mathbf{v}_D ($\tau \approx 1$), (b) \mathbf{v}_L ($\tau \approx 1$) and (c) \mathbf{v}_F ($\tau \approx 1$) computed from pairs of consecutive SDO/HMI intensitygrams with spatial resolution $\Delta x \approx 0.505'' \approx 368$ km per pixel. **Only the arrows of the horizontal velocity vector fields are displayed for clarity reasons.** The continuum intensity I_c ($\tau \approx 1$) measured by SDO/HMI on 8 Oct. 2010 is displayed as background (colorscale).

the procedure described in Section 2. DeepVel computations of the horizontal flow using the resulting continuum images (Figure 7(b)) are less accurate than the results obtained in Section 3.1 (see Tables 2 and 5). This is the case for all reconstruction algorithms (Figures 7(c) and 7(d)). As previously observed, DeepVel best reconstructs the horizontal flow at granular and subgranular scales (Table 5). Therefore, although the neural network’s training process is model-dependent, DeepVel can accurately infer the flow’s amplitude and orientation using results from another numerical simulation as input.

3.5. Velocity Fields Inferred from SDO/HMI Data

With the neural network now properly trained to generate horizontal flows at spatial resolution $\Delta x \approx 0.505'' \approx 368$ km per pixel, we used real intensitygrams measured by SDO/HMI on 8 Oct. 2010 as input in DeepVel. SDO/HMI intensitygrams are separated by $\Delta t = 45$ seconds. The synthetic intensitygrams and velocity fields used to train DeepVel were however separated by $\Delta t = 60$

seconds. Ideally, the neural network should be trained with the correct time step for consistency. **To approximate real SDO/HMI velocities, v_D was rescaled by a factor of 45/60.** Inferred flows (Figure 8(a)) are again consistent with plasma motions associated with small scales features and granulation (see the continuum intensity I_c displayed in the background of Figure 8). LCT and FLCT on the other hand both infer flows on a much larger scale (Figures 8(b) and 8(c)). This is confirmed by the kinetic energy spectra as a function of the wavenumber (Figure 3(b)). DeepVel and FLCT produce similar variations to the ones seen in Figure 3(a) when synthetic SDO/HMI observations were used as input. Accumulation of energy at smaller scales in the LCT spectra (Figure 3(b)) is associated with decorrelated noise and suggests that the algorithm should not be used to reconstruct motions at those scales (Rieutord *et al.*, 2010).

4. Conclusion

We compared horizontal velocity fields inferred from pairs of synthetic intensitygrams at the SDO/HMI spatial resolution using DeepVel, LCT, FLCT and CST to identify which method is best suited to generate synthetic observations for data assimilation in a MHD model. Reconstructions must capture features at spatial and temporal scales that are consistent with real observations as well as the numerical model. Computations should also be done quickly and reliably for use in a reduction pipeline. Only DeepVel can generate instantaneous velocity fields as other methods rely on temporal (and spatial) averaging for increased correlations. Using 30-minute averages, we found that DeepVel best infers granular and subgranular components of the plasma flow. At supergranular scales, we found that FLCT best reconstructs the supergranular component of the flow. We expect however that DeepVel would best perform if trained with data at the corresponding spatial resolution. It was also shown that $k - \omega$ filtering of input data is not a mandatory preprocessing step. Finally, we determined that 30-minute average can be accurately estimated from eight equally-distributed pairs of consecutive continuum images out of the thirty available, hence reducing the number of DeepVel computations performed (and computation time) in a data reduction pipeline preparing synthetic data for data assimilation.

Horizontal velocities inferred by the DeepVel neural network are model-dependent. We however determined that DeepVel can still accurately reconstruct the flow's orientation and amplitude when using input generated from a different numerical simulation (*e.g.* the Rieutord *et al.* (2001) numerical simulation) than the one used for the training process. Model dependency could prove useful when incorporating horizontal velocity fields in a MHD model to perform data-driven simulations or data assimilation. On top of measurement and representation errors, observations may simply not satisfy the model's equations (Abbett and Fisher, 2010). The same can be argued about reconstructions. Training DeepVel using results from the same MHD model used to perform data assimilation should generate synthetic velocity fields that, in comparison, are more consistent with the model. We plan on using DeepVel-inferred horizontal velocities as synthetic observations at multiple optical depths when we attempt data assimilation

of solar granulation in a radiative MHD model of the Sun's upper convection zone to lower corona. If DeepVel were trained with a proper spherical MHD simulation of the photosphere and upper layers (*e.g.* RADMHD2S (Abbett, Bercik, and Fisher, 2014; Abbett and Bercik, 2014)), it could also be used to infer transverse velocities on the limb, a feature other velocity reconstruction algorithms have yet to achieve.

Acknowledgments The authors would like to thank A. Asensio Ramos, I.S. Requerey and N. Vitas for making the DeepVel neural network available to the community as open source (<https://github.com/aasensio/deepvel>). This work was granted access to the HPC resources of CALMIP under allocation 2011-[P11115]. Benoit Tremblay is supported through an FRQNT fellowship and a Mitacs Globalink Research Award. Alain Vincent is supported through an NSERC Individual Research Grant.

References

- Abbett, W.P.: 2007, The Magnetic Connection between the Convection Zone and Corona in the Quiet Sun. *Astrophys. J.* **665**, 1469. DOI. ADS.
- Abbett, W.P., Bercik, D.J.: 2014, RADMHD2S: A Global 3D Radiative-MHD Model of the Upper Convection Zone-to-Corona System. In: *American Astronomical Society Meeting Abstracts #224, AAS Meeting Abstracts* **224**, 123.47. ADS.
- Abbett, W.P., Fisher, G.H.: 2010, Improving large-scale convection-zone-to-corona models. **81**, 721. ADS.
- Abbett, W.P., Fisher, G.H.: 2012, Radiative Cooling in MHD Models of the Quiet Sun Convection Zone and Corona. *Solar Phys.* **277**, 3. DOI. ADS.
- Abbett, W.P., Bercik, D.J., Fisher, G.H.: 2014, Modeling the Convection Zone-to-Corona System over Global Spatial Scales. *AGU Fall Meeting Abstracts*. ADS.
- Asensio Ramos, A., Requerey, I.S., Vitas, N.: 2017, DeepVel: Deep learning for the estimation of horizontal velocities at the solar surface. *Astron. Astrophys.* **604**, A11. DOI. ADS.
- Bobra, M.G., Sun, X., Hoeksema, J.T., Turmon, M., Liu, Y., Hayashi, K., Barnes, G., Leka, K.D.: 2014, The Helioseismic and Magnetic Imager (HMI) Vector Magnetic Field Pipeline: SHARPs - Space-Weather HMI Active Region Patches. *Solar Phys.* **289**, 3549. DOI. ADS.
- Bouttier, F., Courtier, P.: 1999, Data assimilation concepts and methods March 1999, 1.
- Diaz Baso, C.J., Asensio Ramos, A.: 2017, Enhancing SDO/HMI images using deep learning. *ArXiv e-prints*. ADS.
- Espagnet, O., Muller, R., Roudier, T., Mein, N.: 1993, Turbulent power spectra of solar granulation. *Astron. Astrophys.* **271**, 589. ADS.
- Fisher, G.H., Welsch, B.T.: 2008, FLCT: A Fast, Efficient Method for Performing Local Correlation Tracking. In: Howe, R., Komm, R.W., Balasubramaniam, K.S., Petrie, G.J.D. (eds.) *Subsurface and Atmospheric Influences on Solar Activity, Astronomical Society of the Pacific Conference Series* **383**, 373. ADS.
- Hoeksema, J.T., Liu, Y., Hayashi, K., Sun, X., Schou, J., Couvidat, S., Norton, A., Bobra, M., Centeno, R., Leka, K.D., Barnes, G., Turmon, M.: 2014, The Helioseismic and Magnetic Imager (HMI) Vector Magnetic Field Pipeline: Overview and Performance. *Solar Phys.* **289**, 3483. DOI. ADS.
- Jiang, C., Wu, S.T., Feng, X., Hu, Q.: 2016, Data-driven magnetohydrodynamic modelling of a flux-emerging active region leading to solar eruption. *Nature Communications* **7**, 11522. DOI. ADS.
- Longcope, D.W.: 2004, Inferring a Photospheric Velocity Field from a Sequence of Vector Magnetograms: The Minimum Energy Fit. *Astrophys. J.* **612**, 1181. DOI. ADS.
- November, L.J., Simon, G.W.: 1988, Precise proper-motion measurement of solar granulation. *Astrophys. J.* **333**, 427. DOI. ADS.
- Rempel, M.: 2017, Extension of the MURaM Radiative MHD Code for Coronal Simulations. *Astrophys. J.* **834**, 10. DOI. ADS.

- Rempel, M., Cheung, M.C.M.: 2014, Numerical Simulations of Active Region Scale Flux Emergence: From Spot Formation to Decay. *Astrophys. J.* **785**, 90. DOI. ADS.
- Rieutord, M., Roudier, T., Ludwig, H.-G., Nordlund, Å., Stein, R.: 2001, Are granules good tracers of solar surface velocity fields? *Astron. Astrophys.* **377**, L14. DOI. ADS.
- Rieutord, M., Roudier, T., Roques, S., Ducottet, C.: 2007, Tracking granules on the Sun's surface and reconstructing velocity fields. I. The CST algorithm. *Astron. Astrophys.* **471**, 687. DOI. ADS.
- Rieutord, M., Meunier, N., Roudier, T., Rondi, S., Beigbeder, F., Parès, L.: 2008, Solar supergranulation revealed by granule tracking. *Astron. Astrophys.* **479**, L17. DOI. ADS.
- Rieutord, M., Roudier, T., Rincon, F., Malherbe, J.-M., Meunier, N., Berger, T., Frank, Z.: 2010, On the power spectrum of solar surface flows. *Astron. Astrophys.* **512**, A4. DOI. ADS.
- Shou, J., Scherrer, P.H., Bush, R.I., Wachter, R., Couvidat, S., Rabello-Soares, M.C., Bogart, R.S., Hoeksema, J.T., Liu, Y., Duvall, T.L., Akin, D.J., Allard, B.A., Miles, J.W., Rairden, R., Shine, R.A., Tarbell, T.D., Title, A.M., Wolfson, C.J., Elmore, D.F., Norton, A.A., Tomczyk, S.: 2012, Design and Ground Calibration of the Helioseismic and Magnetic Imager (HMI) Instrument on the Solar Dynamics Observatory (SDO). *Solar Phys.* **275**, 229. DOI. ADS.
- Schrijver, C.J., De Rosa, M.L., Metcalf, T.R., Liu, Y., McTiernan, J., Régnier, S., Valori, G., Wheatland, M.S., Wiegmann, T.: 2006, Nonlinear Force-Free Modeling of Coronal Magnetic Fields Part I: A Quantitative Comparison of Methods. *Solar Phys.* **235**, 161. DOI. ADS.
- Schuck, P.W.: 2006, Tracking Magnetic Footpoints with the Magnetic Induction Equation. *Astrophys. J.* **646**, 1358. DOI. ADS.
- Solanki, S.K., Walther, U., Livingston, W.: 1993, Infrared lines as probes of solar magnetic features. VI. The thermal-magnetic relation and Wilson depression of a simple sunspot. *Astron. Astrophys.* **277**, 639. ADS.
- Stein, R.F., Nordlund, Å.: 1998, Simulations of Solar Granulation. I. General Properties. *Astrophys. J.* **499**, 914. DOI. ADS.
- Stein, R.F., Nordlund, Å.: 2012, On the Formation of Active Regions. *Astrophys. J. Lett.* **753**, L13. DOI. ADS.
- Tremblay, B., Vincent, A.: 2015, A Minimum Energy Fit Method to Reconstruct Photospheric Velocity and Magnetic Diffusivity in Active Regions from Observed Magnetograms and Dopplergrams. *Solar Phys.* **290**, 437. DOI. ADS.
- Tremblay, B., Vincent, A.: 2016, Plasma motions and turbulent magnetic diffusivity of active region ar 12158 using a minimum energy functional and non-force-free reconstructions of vector magnetograms. *Solar Physics* **292**(1), 2. DOI.
- Verma, M., Steffen, M., Denker, C.: 2013, Evaluating local correlation tracking using CO5BOLD simulations of solar granulation. *Astron. Astrophys.* **555**, A136. DOI. ADS.
- Vögler, A., Shelyag, S., Schüssler, M., Cattaneo, F., Emonet, T., Linde, T.: 2005, Simulations of magneto-convection in the solar photosphere. Equations, methods, and results of the MURaM code. *Astron. Astrophys.* **429**, 335. DOI. ADS.